



Modeling of the anode of a liquid-feed DMFC: Inhomogeneous compression effects and two-phase transport phenomena



Pablo A. García-Salaberri, Marcos Vera*, Immaculada Iglesias

Dept. de Ingeniería Térmica y de Fluidos, Universidad Carlos III de Madrid, Avda. de la Universidad, 30, 28911 Leganés, Spain

HIGHLIGHTS

- An isothermal two-phase across-the-channel model for liquid-feed DMFCs is presented.
- The model considers inhomogeneous compression of the GDL (non-uniform porosity).
- Effective anisotropic properties of the GDL are evaluated from empirical data.
- The hydrophobic Leverett J-function approach provides physically inconsistent results.
- Empirical $p_c - s$ data reflecting the mixed-wettability of GDLs give much better predictions.

ARTICLE INFO

Article history:

Received 21 February 2013

Received in revised form

19 June 2013

Accepted 25 June 2013

Available online 18 July 2013

Keywords:

DMFC modeling

Anode

Porous layer

Effective properties

Assembly compression

Capillary transport

ABSTRACT

An isothermal two-phase 2D/1D across-the-channel model for the anode of a liquid-feed Direct Methanol Fuel Cell (DMFC) is presented. The model takes into account the effects of the inhomogeneous assembly compression of the Gas Diffusion Layer (GDL), including the spatial variations of porosity, diffusivity, permeability, capillary pressure, and electrical conductivity. The effective anisotropic properties of the GDL are evaluated from empirical data reported in the literature corresponding to Toray carbon paper TGP-H series. Multiphase transport is modeled according to the classical theory of porous media (two-fluid model), considering the effect of non-equilibrium evaporation and condensation of methanol and water. The numerical results evidence that the hydrophobic Leverett J-function approach is physically inconsistent to describe capillary transport in the anode of a DMFC when assembly compression effects are considered. In contrast, more realistic results are obtained when GDL-specific capillary pressure curves reflecting the mixed-wettability characteristics of GDLs are taken into account. The gas coverage factor at the GDL/channel interface also exhibits a strong influence on the gas-void fraction distribution in the GDL, which in turn depends on the relative importance between the capillary resistance induced by the inhomogeneous compression, $R_c (\propto \partial p_c / \partial \epsilon)$, and the capillary diffusivity, $\bar{D}_c (\propto \partial p_c / \partial s)$.

© 2013 Elsevier B.V. All rights reserved.

1. Introduction

The development of liquid-feed Direct Methanol Fuel Cells (DMFCs), a variant of hydrogen PEMFC technology in which the fuel is an aqueous methanol solution, has accelerated over the last years. Although the power densities that can be reached with PEMFCs are higher, liquid-feed DMFCs present two major advantages compared with PEMFCs: the easier delivery and storage of liquid methanol solutions, and the higher volumetric energy

density of liquid methanol [1–3]. These characteristics make DMFCs a promising candidate as a power source for portable electronic applications, including cell phones, laptop computers, military equipment, etc. [4,5].

However, widespread commercialization of DMFCs is still hindered by several technological problems, such as the slow kinetics of the Methanol Oxidation Reaction (MOR) at the anode Catalyst Layer (CL) and the cathode mixed potential associated with the oxidation of methanol that crosses over the polymer membrane from anode to cathode [6]. Furthermore, the interplay between mass/charge/heat transport, electrochemical kinetics, inhomogeneous compression effects, interfacial contact resistances, and two-phase transport phenomena makes it difficult to achieve optimum design and operating conditions [7]. Thorough study of these

* Corresponding author. Tel.: +34 91 624 9987; fax: +34 91 624 9430.

E-mail addresses: marcos.vera@uc3m.es, m_vera_c@hotmail.com (M. Vera).

URL: <http://fluidos.uc3m.es/people/mvcoello>

complex and interrelated phenomena is therefore necessary from both the experimental and the modeling points of view [8].

One key element affecting fuel cell performance is the Gas Diffusion Layer (GDL). It provides several functions: a pathway for reactant access and excess product removal to/from the CLs, high electrical and thermal conductivity, and adequate mechanical support. In order to fulfill these requirements, GDLs are typically made of porous carbon paper or woven cloth [9]. Both media are characterized by exhibiting significant structural anisotropy due to the preferential orientation of carbon fibers, which typically results in different transport properties along the in-plane and through-plane directions [10]. In addition, the high porosity of these materials provides to the GDL a characteristic soft and flexible structure, susceptible of large deformations when subjected to compression [11]. This introduces important variations in the effective transport properties between the regions under the channel and under the rib when the fuel cell is assembled [8,12–15].

Even though the fundamental role of the GDL has long been recognized by the fuel cell community [16–18], most models presented in the literature to date assume homogenous and isotropic GDL properties. However, this situation has changed during the last few years, and a larger effort is now devoted to the development of more comprehensive models reflecting the real characteristics and operating conditions of the GDLs [19]. Thus, different aspects such as the inhomogeneities caused by the assembly compression and manufacturing process, as well as the inherent anisotropy of the GDL, have been recently incorporated into numerical models. In addition, numerous experimental and numerical works exploring the effective transport properties of GDLs are now available in the literature [20]. This trend should be reinforced in the near future.

The influence of GDL inhomogeneities and anisotropic properties on PEMFC operation has been explored in several modeling works [21–25]. However, these phenomena have been traditionally ignored in DMFC modeling studies (see, e.g., [5,26,27] and references therein), and only a few works can be found in the open literature. Möst et al. [28] presented an analysis of the diffusive mass transport in the anode GDL of a DMFC. In this work, the anisotropic dry diffusivities of different GDLs at various compression ratios were measured, and subsequently employed in Monte Carlo simulations taking into account inhomogeneous compression effects. The limiting current densities predicted by this single-phase model were in qualitative agreement with those obtained experimentally, but a systematic overestimation was observed. Miao et al. [29] developed a two-phase 2D across-the-channel model of a DMFC to investigate the effects of GDL anisotropic properties, inhomogeneous compression, and electrical and thermal contact resistances. These phenomena were taken into account by considering the empirical data reported by Himanen et al. [8,13–15] as a function of the in-plane coordinate x . They concluded that the anisotropy of the GDL has a significant effect on the distribution of species concentration, overpotential, current density, and temperature; even though the isotropic and anisotropic models lead to very similar polarization curves. They also observed that the electrical contact resistance at the CL interface and the GDL compression both play an important role in determining cell performance. In a subsequent work, Miao et al. [30] presented an upgraded version of this model, in which anisotropic heat transfer coefficients were used to capture a more realistic heat transport mechanism. This study was exclusively focused on the influence of GDL anisotropic properties, inhomogeneous compression and contact resistances on heat generation and transport processes. They found that these phenomena have a strong impact on heat transfer processes in DMFCs. Using a model similar to that presented in Ref. [29], He et al. [31] investigated the behavior of water transport through the MEA. The numerical results showed that both the channel-rib pattern and the

deformation of the GDL can cause an uneven distribution of the water-crossover flux along the in-plane direction. In addition, they concluded that both the contact angle and the permeability of the cathode GDL can significantly influence the water-crossover flux.

The effect of assembly compression on the performance of both active and passive DMFCs has been also stressed in a few experimental works [32,33]. Even though the number of studies related to DMFCs is notably lower compared to those available for PEMFCs [32,34–37], these results are far enough to visualize the importance of assembly pressure on DMFC operation. Nevertheless, it would be interesting to explore a wider range of operating conditions and MEA configurations (particularly different type and thicknesses of the GDL) in future experimental work.

The above literature review shows the large impact that GDL inhomogeneous compression and anisotropic properties have on mass/charge/heat transport in DMFCs, thereby affecting fuel cell performance and lifetime. These phenomena should be investigated by physically sound mathematical models including detailed descriptions of the transport processes that occur in the GDL [27].

The present work presents an isothermal two-phase 2D/1D across-the-channel model for the anode of a liquid-feed DMFC. The model takes into account the spatial variations induced by the inhomogeneous assembly compression of the GDL, as well as the inherent anisotropic properties of this key element of the cell. The assembly process is simulated by a novel Finite Element Method (FEM) model, which fully incorporates the nonlinear orthotropic mechanical properties of the GDL (Toray[®] carbon paper TGP-H series) [11]. The resulting porosity distribution is then used to evaluate the effective transport properties of the GDL, i.e., mass diffusivity, permeability, capillary pressure and electrical conductivity, through empirical data reported in the literature. Conceived as an extension of our previous research activity on DMFCs [6], the present model brings new light on the potential influence of GDL inhomogeneous compression on capillary transport processes and gas saturation distribution in the anode of liquid-feed DMFCs. In its present form, the 2D/1D across-the-channel model constitutes a first step towards the development of a full 3D-model for DMFCs that properly takes into account the influence of inhomogeneous compression effects on multiphase transport phenomena.

2. Numerical model

The 2D/1D DMFC model presented in this work is based on the 3D/1D single-phase model previously proposed by Vera [6]. The 3D geometry of the anode has been reduced to a 2D across-the-channel GDL section, while the single-phase 1D model, comprising the catalyst layers, the membrane, and the cathode GDL, presents only minor changes with respect to that presented in Ref. [6]. As major improvements, the upgraded 2D anode model takes into account multiphase transport phenomena according to the classical theory of porous media (two-fluid model), retaining the effect of non-equilibrium phase change of methanol/water. It also includes the effects of the inhomogeneous compression of the GDL, incorporated through the non-uniform porosity distribution obtained from a previous analysis of the GDL compression process [11]. Specifically, the model makes extensive use of empirical correlations of anisotropic carbon paper-based GDLs to evaluate the resulting non-uniform diffusivity, permeability, capillary pressure and electrical conductivity fields induced by the assembly pressure. Finally, the GDL electronic potential is now solved, with the possibility of including the effect of non-uniform contact resistances at the GDL/Rib and GDL/CL interfaces as boundary conditions. The main contribution of this work is to explore the potential impact of GDL inhomogeneous assembly compression on two-phase capillary transport in the anode of a DMFC. The mathematical formulation of

the model can be found in the [Appendix](#), along with all physico-chemical properties and parameters (see [Table A.1](#)). The main assumptions, geometry, constitutive relations (effective properties and phase change source terms), and the main steps followed for the numerical implementation of the model are presented below.

2.1. Assumptions

The present model is based on several simplifying hypotheses that define its limits of validity. The most relevant assumptions specific to the model presented herein are as follows: i) mass transport limitations and flooding phenomena at the cathode are small; ii) the temperature is constant throughout the cell; iii) contact resistances are negligible for the GDL compression ratio considered in this work ($CR = 20\%$); iv) the porosity of the uncompressed GDL (and CL) is homogenous (i.e., the through-plane variations of the porosity of the GDL inherent to the manufacturing process and the PTFE treatment [39–42] are not taken into account); v) the assembly compression does not alter the physicochemical properties of the catalyst layer and the polymer membrane; vi) the gas saturation in the anode catalyst layer does not reduce the catalyst active surface area; vii) carbon dioxide is only present in the gas phase; viii) the saturation profile at the GDL/CL interface is continuous. The remaining assumptions made in this work are common to other DMFC modeling studies and can be found elsewhere [3,6].

Notice that assumption viii) is physically inconsistent according to the theory of porous media [43]. It is capillary pressure rather than saturation the physical variable that must be continuous at the GDL/CL interface. However, the high uncertainty found in the experimentally reported capillary pressure curves of the CL, particularly the high sensitivity to the presence of cracks [44], made us choose a more conservative approach. To date, all the modeling publications that assume a continuous pressure profile at the GDL/CL interface make use of the Leverett J-function approach. The availability of analytical expressions for the p_c – s curves of the GDL and CL makes then easier to impose the physically sound condition of continuous capillary pressure at the GDL/CL interface. However, as will be discussed in Section 2.6, the applicability of the Leverett approach has been challenged by numerous experimental studies, and should also be reconsidered in future fuel cell modeling efforts.

2.2. Geometry

We shall assume a parallel channel configuration for the anode flow-field. Accordingly, the domain under study is restricted to the region between the mid-plane of one channel and that of the neighboring rib to reduce computational cost. Symmetry boundary conditions are considered at both boundaries. As depicted in [Fig. 1](#), the computational domain includes the five layers composing the MEA, i.e., the anode gas diffusion layer (agdl), the anode catalyst layer (acl), the polymer electrolyte membrane (mem), the cathode catalyst layer (ccl), and the cathode gas diffusion layer (cgdl). The geometry of the anode 2D model is defined by four geometrical parameters, namely the rib half-width, w_{rib} , the uncompressed GDL thickness, δ_{agdl} , the distance between the rib and channel symmetry planes, w_{agdl} , and the fillet radius of the rib, r_{rib} . The geometry of the 1D model (catalyst layers, membrane and cathode GDL) is simply defined by the thickness of the different layers; δ_{acl} and δ_{ccl} for the anode and cathode catalyst layers, respectively, δ_{mem} for the polymer membrane, and δ_{cgdl} for the cathode GDL. The value of the geometric dimensions has been kept constant throughout the work; $w_{agdl} = 1$ mm, $w_{rib} = 0.5$ mm, $r_{rib} = 40$ μ m, $\delta_{agdl} = \delta_{cgdl} = 190$ μ m (Toray[®] carbon paper TGP-H-060), $\delta_{acl} = \delta_{ccl} = 30$ μ m, $\delta_{mem} = 178$ μ m (Nafion[®] 117).

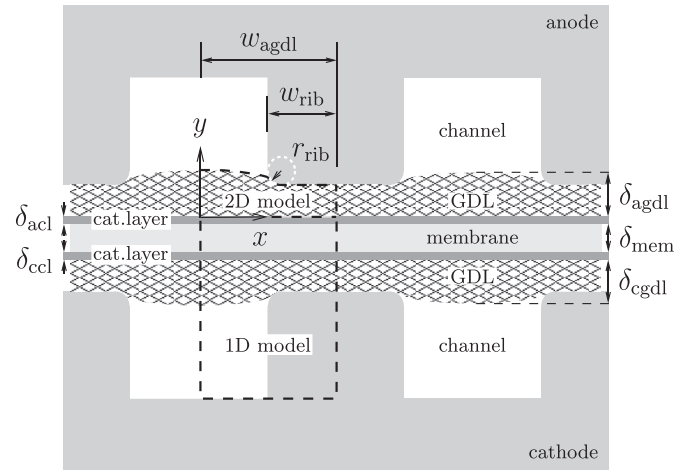


Fig. 1. Schematic of the modeling domains covered by the 2D and 1D models showing the coordinate system, and the notation used for the anode rib-half width, w_{rib} , the distance between the anode rib and channel symmetry planes, w_{agdl} , the fillet radius of the anode rib, r_{rib} , and the thickness of the different layers of the MEA.

2.3. Effective diffusivity

Following the approach of Nam and Kaviani [45], the effective diffusivity of species i in the GDL under multiphase flow conditions, $D_{ij}^{eff,wet}$, where $j = l/g$ denotes liquid/gas phase, respectively, is correlated with porosity (dry diffusivity) and saturation (relative diffusivity) through the normalized functions $f(\epsilon)$ and $g_j(s)$, defined as

$$\frac{D_{ij}^{eff,wet}}{D_{ij}^{bulk}} = \underbrace{\frac{D_{ij}^{eff,dry}}{D_{ij}^{bulk}}}_{f(\epsilon)} \underbrace{\frac{D_{ij}^{eff,wet}}{D_{ij}^{eff,dry}}}_{g_j(s)} = f(\epsilon)g_j(s) \quad (1)$$

where D_{ij}^{bulk} is the bulk diffusivity of species i in phase j .

To account for the influence of compression on the dry, or single-phase, diffusivity, $D_{ij}^{eff,dry}$, we have considered the experimental data reported by Flückiger et al. [46,47] and Möst et al. [28]. Both works show good agreement between them and with other experimental [48,49], numerical [50–52], and analytical [53] studies presented in the literature. A good fit to the reported in-plane (ip) and through-plane (tp) experimental values for carbon paper TGP-H-060 with different PTFE contents (0–40 wt.%) over the porosity range $0.3 < \epsilon < 0.8$ is provided by the following exponential functions [11]:

$$f^{ip}(\epsilon) = \frac{D_{ij}^{eff,dry,ip}}{D_{ij}^{bulk}} = 2.92 \times 10^{-2} \exp(3.80\epsilon) \quad (2a)$$

$$f^{tp}(\epsilon) = \frac{D_{ij}^{eff,dry,tp}}{D_{ij}^{bulk}} = 6.51 \times 10^{-3} \exp(5.02\epsilon) \quad (2b)$$

Notice that due to the in-plane arrangement of the fibers the pores are preferentially oriented in this direction, resulting in a higher effective in-plane dry diffusivity, $D_{ij}^{eff,dry,ip} > D_{ij}^{eff,dry,tp}$. Indeed, the degree of anisotropy is about 2, and increases as the GDL is compressed due to the realignment of fibers [11,47].

The influence of liquid/gas saturation on the effective diffusivity, given by the relative diffusivity, has been modeled according to the

isotropic Bruggeman's effective medium theory [54], as typically employed in fuel cell modeling studies:

$$g_l^{\text{ip/tp}}(s) = \frac{D_{ij}^{\text{eff,wet,ip/tp}}}{D_{ij}^{\text{eff,dry,ip/tp}}} = s^{1.5} \quad (3a)$$

$$g_g^{\text{ip/tp}}(s) = \frac{D_{ij}^{\text{eff,wet,ip/tp}}}{D_{ij}^{\text{eff,dry,ip/tp}}} = (1-s)^{1.5} \quad (3b)$$

Although there are several experimental [55,56] and numerical [45,52,57,58] works related to the impact of water saturation on the effective diffusivity of the GDL in PEMFCs, there is a lack of knowledge on the effects of the two-phase flow conditions that prevail in the anode of a DMFC. In general, a large research effort is still needed to incorporate realistic descriptions reflecting the particular multiphase characteristics of GDLs. Particularly, the influence of GDL anisotropy and compression on multiphase properties should be further investigated in order to improve the predictive capabilities of numerical models. For the time being, the Bruggeman correction has been considered a good starting point in this work.

2.4. Absolute and relative permeability

The impact of compression on the absolute permeability is taken into account according to the experimental data reported by Flückiger [47] corresponding to carbon paper TGP-H-060 with 0–20 wt.% PTFE over the porosity range $0.6 < \varepsilon < 0.8$. The values reported in Ref. [47] are in the range of other empirical data presented in the literature [59–61] and the analytical model recently proposed by Tamayol et al. [62,63]. The analytical expressions obtained by fitting the reported in-plane and through-plane experimental data to exponential functions are as follows:

$$K^{\text{ip}}(\varepsilon) = 2.52 \times 10^{-16} \exp(14.65\varepsilon) \quad [\text{m}^2] \quad (4a)$$

$$K^{\text{tp}}(\varepsilon) = 2.30 \times 10^{-16} \exp(12.51\varepsilon) \quad [\text{m}^2] \quad (4b)$$

It is worth noting that the degree of anisotropy of the absolute permeability is in general higher than that observed for the dry diffusivity. Thus, the ratio between the values along the in-plane and through-plane direction is between 2 and 5 in the porosity range measured by Flückiger [47]. Interestingly, the degree of anisotropy of the absolute permeability decreases with increasing compression as opposite to the dry diffusivity.

To account for the influence of liquid/gas saturation, we have considered the third-order empirical correlation for the relative permeability originally developed for well-sorted unconsolidated sand [64]:

$$k_{rg}^{\text{ip/tp}}(s) = (1-s)^3 \quad (5a)$$

$$k_{rl}^{\text{ip/tp}}(s) = s^3 \quad (5b)$$

Although this correlation is usually adopted in fuel cell modeling studies, it should be noted that its applicability to fibrous GDLs has been debated many times. Nowadays, several GDL-specific experimental data can be found in the literature [61,65–67]. However, the measurements are subject to high uncertainty and the liquid saturation levels explored in them are quite small so as to reach a firm conclusion for the conditions typically present in the anode of a DMFC. As noted above for the relative diffusivity, experimental

and numerical work is still necessary to incorporate more realistic characterizations into continuum-based numerical models.

2.5. Electrical conductivity

The effective electrical conductivity has been correlated to the experimental data reported by Flückiger [47] and Reum [68] for carbon paper TGP-H-060 with 20 wt.% PTFE over the porosity range $0.6 < \varepsilon < 0.8$:

$$\sigma^{\text{eff,ip}}(\varepsilon) = 48221 - 46729\varepsilon \quad [\text{S/m}] \quad (6a)$$

$$\sigma^{\text{eff,tp}}(\varepsilon) = 6582 - 7229\varepsilon \quad [\text{S/m}] \quad (6b)$$

The degree of anisotropy of the electrical conductivity is even higher than that observed for the dry diffusivity and the absolute permeability. The in-plane values are about one order of magnitude higher than the values in the through-plane direction. As opposite to mass transport properties, the electrical conductivity increases as the GDL is compressed due to the larger number of contact points among fibers. In particular, the in-plane conductivity increases linearly with decreasing thickness so that the in-plane resistance remains almost constant [69].

2.6. Capillary pressure–saturation relationship

One key property affecting two-phase transport phenomena which deserves further attention is the capillary pressure–saturation relationship, p_c – s . Most of the multiphase models developed for PEM fuel cells, either PEMFCs or DMFCs, usually adopt the semi-empirical correlation originally proposed by Leverett [70], and subsequently modified by Rose and Bruce [71] with the intent to capture wettability effects:

$$p_c(s, \varepsilon) = p_g - p_l = \sigma \sqrt{\frac{\varepsilon}{K(\varepsilon)}} \cos(\theta_c) J(s) \quad (7)$$

where σ is the surface tension of the immiscible fluid pair, ε and K are the porosity and absolute permeability of the porous media, respectively, θ_c is the contact angle between both phases, and $J(s)$ is the so-called Leverett J-function. Note that the capillary pressure has been defined in this work as $p_c = p_g - p_l$. Since the seminal work of Wang et al. [72], a common practice in the modeling community is to use as Leverett J-function the polynomial fit to Leverett's experimental data proposed by Udell [73]:

$$J(s) = \begin{cases} 1.4(1-s) - 2.1(1-s)^2 + 1.3(1-s)^3 & \theta_c < 90^\circ \\ 1.4s - 2.1s^2 + 1.3s^3 & \theta_c > 90^\circ \end{cases} \quad (8)$$

The contact angle in this expression is assumed to be around 100° to account for the hydrophobic characteristics of PTFE-treated GDLs. As a result, the capillary pressure is negative, i.e., p_g is less than p_l , over the entire range of liquid saturation.

However, the applicability of this modeling approach to GDLs has been questioned many times [74–81], and may be especially erroneous under the two-phase flow conditions existing in the anode of a DMFC. GDL-specific experimental data for the water–air fluid pair have shown that gas diffusion layers present mixed-wettability characteristics and display permanent hysteresis between imbibition (water displaces air) and drainage (air displaces water) processes. Based on these findings, it should be expected that capillary transport of gas-phase bubbles in the anode of a DMFC is better described by the p_c – s curve associated with the drainage process, i.e., gas phase displaces liquid phase, while capillary transport of liquid-phase droplets in the cathode of a DMFC or a PEMFC is

represented more adequately by the p_c – s curve associated with the imbibition process, i.e., liquid phase displaces gas phase.

In comparison with the hydrophobic Leverett J-function approach ($\theta_c > 90^\circ$), GDL-specific experimental data present obvious differences in shape and magnitude. However, a more fundamental difference arises in the sign of the capillary pressure. Whereas experimental imbibition curves agree qualitatively with the hydrophobic Leverett J-function and show negative capillary pressures in almost the entire range of liquid saturation, experimental drainage curves do not reflect this behavior, and the capillary pressure is positive (see, e.g., [75] and references therein). Moreover, the influence of compression is exactly the opposite. While the hydrophobic Leverett J-function approach predicts increasing negative capillary pressures as the GDL is compressed, i.e., for lower porosity, GDL-specific drainage data are displaced to higher, i.e., more positive, capillary pressures. This contradictory situation can be observed in Fig. 2, where the p_c – s curves predicted by the hydrophobic Leverett J-function approach ($\theta_c = 100^\circ$) and GDL-specific drainage data [74] are shown for different GDL porosities. The opposite behavior of both approaches suggests that the applicability of fully hydrophobic relationships may be physically incorrect to describe capillary transport in the anode of a DMFC. A detailed analysis of this topic is presented below in Section 3.

The experimental drainage data used in this work to describe the capillary pressure–saturation relationship correspond to the measurements reported by Gostick et al. [74] for TGP-H-120 (10 wt.% PTFE) using the water–air fluid pair. In Ref. [74] the p_c – s curves associated with an uncompressed GDL and a 30% compressed GDL were presented. Even though the measurements were not exclusively adapted to the two-phase system present in the anode of a DMFC, these data can be considered as a good starting point for the exploratory purpose of this work. Future work should be carried out to obtain a more detailed description of capillary pressure as a function of GDL compression. Also of interest would be to investigate the influence of additional variables that may lead to Gibbs-Marangoni effects, such as the concentration of methanol or the temperature.

The van Genuchten-type equation proposed by Gostick et al. [74] to describe the experimental drainage curves is as follows:

$$p_c(s) = p_g - p_l = p_{c,b} \left[\left(\frac{s - s_r}{1 - s_r} \right)^{-1/n} - 1 \right]^{1/m} - p_{ref} \quad (9)$$

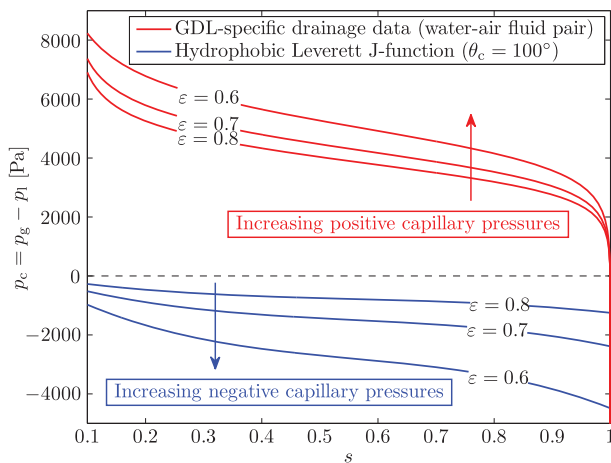


Fig. 2. Capillary pressure–saturation relationship, p_c – s , predicted by the hydrophobic Leverett J-function approach ($\theta_c = 100^\circ$) and GDL-specific drainage data [74]. The different curves correspond to different values of porosity, ϵ . The dependence of the capillary pressure on porosity was obtained following the procedure presented in this section.

The value of the different parameters appearing in this equation can be found in Ref. [74].

To account for the effect of GDL compression on capillary pressure we performed a linear interpolation between the two p_c – s curves reported by Gostick et al. [74]. The inverse of the characteristic pore radius, r_p^{-1} , was considered as the representative variable to perform the interpolation, i.e.,

$$p_c(s, r_p^{-1}) = \beta p_c^u(s) + (1 - \beta) p_c^c(s); \quad \beta = \frac{r_p^{-1} - (r_p^{-1})^c}{(r_p^{-1})^u - (r_p^{-1})^c} \quad (10)$$

where $p_c^u(s)$ and $p_c^c(s)$ are the p_c – s curves associated with the uncompressed and 30% compressed GDLs, respectively.

According to Leverett [70], the characteristic pore radius was calculated as:

$$r_p(\epsilon) = \sqrt{\frac{K_{avg}(\epsilon)}{\epsilon}} \quad (11)$$

where $K_{avg}(\epsilon) = [K^{ip}(\epsilon) + K^{tp}(\epsilon)]/2$ is the average value of the absolute permeability. Note that, as it should be expected, with the expressions for $K^{ip}(\epsilon)$ and $K^{tp}(\epsilon)$ given in Eq. (4) the characteristic pore radius decreases with decreasing porosity (that is, with increasing GDL compression). In the simulations performed with the Leverett J-function approach, Eqs. (7) and (8), the inverse of the characteristic pore radius, $r_p^{-1} = \sqrt{\epsilon/K(\epsilon)}$, was calculated in the same way.

To compute the characteristic pore radius of the compressed PTFE-treated GDL, r_p^c , the porosity was calculated based on the thickness compression ratio, CR, using the following expression:

$$\epsilon^c = \frac{\epsilon^u - CR}{1 - CR}; \quad CR = \frac{\Delta\delta}{\delta^u} \quad (12)$$

derived by assuming that the change of thickness experienced by the GDL is due solely to the decrease of pore volume. Here, $\Delta\delta$ is the reduction of the GDL thickness, and δ^u and ϵ^u are the uncompressed GDL thickness and porosity, respectively. These values were reported by Gostick et al. [74]. The characteristic pore radius of the uncompressed GDL, r_p^u , was directly obtained from the value of the uncompressed GDL porosity given in Ref. [74].

2.7. Phase change source terms

Most of the published models for DMFCs which consider non-equilibrium phase change phenomena assume different descriptions for the phase change rate of methanol and water (see, e.g., [3,29–31,82]). However, except for the fact that both expressions were developed by different authors, no arguments can be found in the literature to justify these differences.

Specifically, the evaporation/condensation rate of methanol is often modeled according to the expression originally proposed by Divisek et al. [83]:

$$\dot{R}_m = A_{lg} h_{lg} s(1 - s) (C_m^{sat} - C_{mv}) \quad (13)$$

where the phase change rate is proportional to the product of the liquid and the gas saturation, s and $(1 - s)$, respectively, and the driving-force is the difference between the concentration of methanol vapor, C_{mv} , and the saturation concentration of methanol, C_m^{sat} . A_{lg} and h_{lg} denote the specific interfacial area and the interfacial transfer coefficient between the liquid and the gas phase in the porous media, respectively. Both parameters are assumed constant in numerical models.

On the other hand, since the original work of Murgia et al. [84], the phase change rate of water is usually modeled using a formulation similar to that employed in PEMFC modeling studies [85]:

$$\dot{R}_w = \begin{cases} k_{\text{evp}} \frac{\varepsilon s \rho_l}{M_w} (p_w^{\text{sat}} - p_{\text{wv}}) & p_{\text{wv}} < p_w^{\text{sat}} \\ k_{\text{con}} \frac{\varepsilon (1-s) X_{\text{wv}}}{RT} (p_w^{\text{sat}} - p_{\text{wv}}) & p_{\text{wv}} > p_w^{\text{sat}} \end{cases} \quad (14)$$

where ε is the porosity, ρ_l is the density of liquid water, M_w is the molecular weight of water, X_{wv} is the mole fraction of water vapor in the gas phase, T is the operating temperature, and R the universal gas constant. The driving-force is the difference between the partial pressure of water vapor, p_{wv} , and the saturation pressure of water, p_w^{sat} . In the above expressions, k_{evp} and k_{con} denote the evaporation and condensation rate constants, respectively. The basis of this formulation is physically more meaningful. The expressions for the evaporation and condensation processes are differentiated, so that the interfacial mass-transfer associated with each phenomenon is proportional to the amount of species per unit volume governing that process, i.e., liquid-phase species for the evaporation process and gas-phase species for the condensation process.

In the present work, the phase change rate of methanol and water has been formulated under a common modeling framework, following the same physical principles considered in PEMFC modeling studies. Thus, the expression proposed for the phase change rate of methanol ($i = m$) and water ($i = w$) is as follows:

$$\dot{R}_i = \begin{cases} k_{\text{evp}} \frac{\varepsilon s X_{il} \rho_l}{M_w} (p_i^{\text{sat}} - p_{iv}) & p_{iv} < p_i^{\text{sat}} \\ k_{\text{con}} \frac{\varepsilon (1-s) X_{iv}}{RT} (p_i^{\text{sat}} - p_{iv}) & p_{iv} > p_i^{\text{sat}} \end{cases} \quad (15)$$

where X_{il} is the mole fraction of methanol/water in the liquid phase and X_{iv} is the mole fraction of methanol/water vapor in the gas phase.

In a first approximation, we have assumed that the evaporation and condensation rate constants of both methanol and water are equal. This hypothesis results from the assumption that the underlying physical characteristics of the heat and mass transfer phenomena governing the phase change processes are similar for both species. The only difference arising between the evaporation and condensation rate of methanol and water is attributed to the different amount of each species present in the porous media. For the diluted methanol solutions typically employed in liquid-feed DMFCs, this modeling approach indeed reflects that water is closer to thermodynamic equilibrium conditions, as it should be expected [86]. The values of the evaporation and condensation rate constants have been estimated from those previously presented in the literature and are listed in Table A.1. It should be pointed out that this modeling approach is only an alternative to previous formulations employed in numerical models to describe non-equilibrium phase change phenomena. As considered in other modeling studies [1,86,87], the assumption that both methanol and water are in thermodynamic equilibrium corresponds to the limit $k_{\text{evp}}, k_{\text{con}} \rightarrow \infty$.

2.8. Numerical implementation

As a first step in our multiphysics modeling approach, the inhomogeneous assembly compression of the GDL was simulated using a novel FEM model [11] implemented in the commercial code ABAQUS®/Standard [88]. The assembly process was modeled by imposing a specified GDL compression ratio, CR, expressed as a percentage of its initial thickness. For further details, the reader is

referred to Ref. [11]. Then, the deformed mesh of the GDL and the associated porosity distribution were imported into the commercial finite-volume-based code ANSYS® FLUENT 13.0 [89]. This CFD code was used to solve the different conservation equations, complemented with numerous User Defined Functions (UDFs). The UDFs were employed to customize different aspects of the model, including governing equations, boundary conditions, source terms, effective properties, model parameters, etc. Further details about the numerical procedure followed to couple the 2D/1D model can be found in Ref. [6]. The number of quadrilateral elements/cells employed in the simulations performed in both ABAQUS® and ANSYS® FLUENT was 7600, corresponding to an element/cell size of 5 μm . Grid refinement studies confirmed that this level of refinement was appropriate to accurately describe the inhomogeneities induced by the assembly compression without excessively increasing the computational cost.

2.9. Numerical validation

Before proceeding further, we checked the ability of the model to reproduce the numerical results found in the literature. In a real fuel cell both reactant/product concentrations and liquid/gas saturation evolve along the channel, so that polarization curves obtained with our 2D across-the-channel model could not be strictly compared with any experimentally observed I–V curve. This is also the case in other 2D across-the-channel models, such as the one proposed by Yang and Zhao [3], which will be used here for comparative purposes. To mimic the modeling assumptions of Ref. [3], we considered an undeformed GDL with homogenous porosity and isotropic properties with a Bruggeman-type correction for the dry diffusivity, i.e., $f_{l/g}^{\text{tp}}(\varepsilon) = \varepsilon^{1.5}$. In addition, the Leverett J-function approach, Eqs. (7) and (8), with $\theta_c = 100^\circ$ was used to describe the p_c – s relationship, and Eqs. (13) and (14) were employed to model the phase change rates of methanol and water. The value of the geometrical dimensions and operating conditions were also adapted to that employed by Yang and Zhao [3]. Despite all these modifications, the resulting baseline model still presents some fundamental differences with the model by Yang and Zhao [3], such as the formulation of the MOR electrochemical kinetics, the consideration of a global electrical contact resistance or the description of mass transport processes in the cathode GDL. Nevertheless, the purpose of this validation was not to establish a one-to-one comparison, but to check the ability of our model to provide similar results to those previously reported in the literature. The spatial distributions of liquid methanol concentration, C_{ml} , methanol vapor concentration, C_{mv} , and gas-void fraction, $1-s$, predicted by the present model are shown in Fig. 3. As compared to the numerical results reported by Yang and Zhao [3, Fig. 4], it can be seen that both models exhibit good qualitative agreement. The numerical discrepancies between them should be attributed to the differences discussed above.

3. Results and discussion

3.1. Hydrophobic Leverett J-function vs. GDL-specific experimental drainage data

An interesting finding emerges when the numerical results obtained with the hydrophobic Leverett J-function ($\theta_c > 90^\circ$) are compared to those obtained using GDL-specific drainage data. In the presence of inhomogeneous compression effects, both approaches lead to gas-phase velocities with completely different orientations. This opposite behavior, illustrated in Fig. 4, is explained based on Darcy's law for the gas phase, Eq. (A.5). As it is well-known, this law states that the gas-phase velocity is

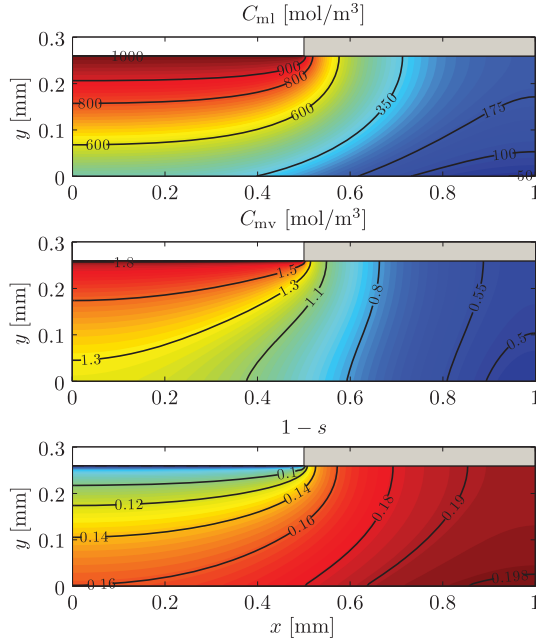


Fig. 3. Molar concentration of liquid methanol, C_{ml} , molar concentration of methanol vapor, C_{mv} , and gas-void fraction, $1-s$, predicted by the present model as compared to the numerical results presented by Yang and Zhao [3] (Fig. 4).

proportional to the pressure gradient of the gas phase ($\mathbf{u}_g \propto \nabla p_g$). However, since the pressure gradient that is necessary to drive the convective flow of the liquid phase is rather small, the gas-flow is essentially dominated by the capillary pressure gradient, $\nabla p_g = \nabla p_l + \nabla p_c \approx \nabla p_c$, so that $\mathbf{u}_g \propto \nabla p_c$.

This can be checked by comparing the order of magnitude of the liquid-phase pressure gradient, ∇p_l , with the characteristic capillary pressure gradient, ∇p_c , across the GDL. The order of magnitude of the liquid-phase pressure gradient is estimated according to Darcy's law for the liquid phase, Eq. (A.3):

$$|\nabla p_l| \sim \frac{\mu_l}{K_{avg} k_{rg}} |\mathbf{u}_l| \quad (16)$$

On the other hand, the characteristic value of the capillary pressure gradient can be estimated from the capillary pressure drop between the virtually uncompressed region under the channel and the compressed region under the rib, $\Delta p_c^{cha/rib}$. Using the thickness of the GDL, $\delta_{agdl} \sim \mathcal{O}(10^{-4})$ m, as characteristic length, this leads to

$$|\nabla p_c| \sim \frac{\Delta p_c^{cha/rib}}{\delta_{agdl}} \quad (17)$$

Thus, comparing the order of magnitude of both pressure gradients, it turns out that:

$$\frac{|\Delta p_l|}{|\nabla p_c|} \sim \mathcal{O}(10^{-4}/10^{-3}) \quad (18)$$

To get this result we estimated the different properties and parameters by considering a liquid saturation level $s = 0.75$, an average porosity $\varepsilon = 0.74$, and an operating temperature $T = 80^\circ\text{C}$. The velocity of the liquid phase, $|\mathbf{u}_l|$, was estimated from boundary condition (A.12a). In this expression, the fluxes of liquid methanol and water at the GDL/CL interface, N_{ml} and N_{wl} , respectively, were calculated from Eqs. (A.13d), (A.13e) and (A.13f), assuming a typical current density, $i \sim \mathcal{O}(10^2/10^3)$ A/m², and a liquid methanol concentration at the GDL/CL interface, $C_{ml,acI} \sim \mathcal{O}(10/10^2)$ mol/m³. This estimations provided a characteristic liquid-phase velocity, $|\mathbf{u}_l| \sim \mathcal{O}(10^{-7}/10^{-6})$ m/s, that was consistent with the values obtained in the numerical simulations. On the other hand, the capillary pressure drop across the GDL, $\Delta p_c^{cha/rib}$, was computed from Eq. (10) considering a porosity $\varepsilon = 0.76$ for the region under the channel and $\varepsilon = 0.72$ for the region under the rib. The liquid saturation level, $s = 0.75$, was assumed equal in both regions as a first approximation.

Due to the dominant role of the capillary pressure gradient, the increasing negative capillary pressures predicted by the Leverett J-function as the GDL is compressed (i.e., for lower porosities, see Fig. 2) lead to an unrealistic gas-flow towards the more compressed

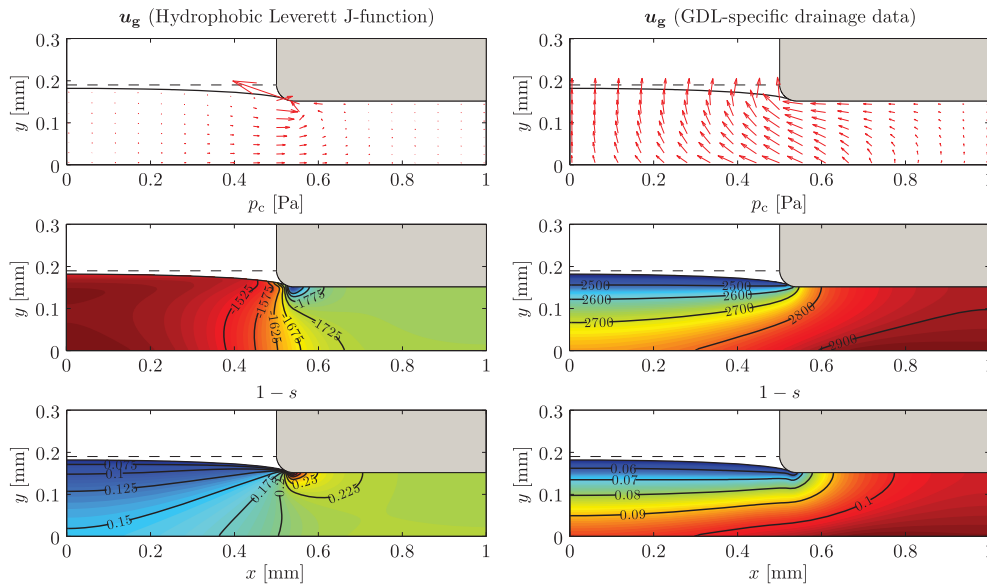


Fig. 4. Gas-phase velocity, \mathbf{u}_g , capillary pressure, p_c , and gas-void fraction, $1-s$, as predicted by considering the hydrophobic Leverett J-function approach ($\theta_c = 100^\circ$) (left), and GDL-specific drainage data [74] (right). The velocity field associated with the hydrophobic Leverett J-function is scaled by a factor of 3 to facilitate its visualization. Operating conditions: $V = 0.25$ V, $CR = 20\%$, $s^{in} = 0.95$, $C_{ml}^{in} = 1$ M, $T = 80^\circ\text{C}$.

region under the rib. Note that the disordered structure of the velocity field under the rib corner seen in Fig. 4 is due to the high porosity reduction and the corresponding large capillary pressure gradients that appear in this region of concentrated stresses. Accordingly, a local mesh refinement would be necessary to increase the spatial resolution in this area. By way of contrast, the increasing positive capillary pressures associated with GDL-specific drainage data as the GDL is compressed (see Fig. 2) lead to a more realistic gas-flow towards the virtually uncompressed region under the channel. This situation can also be observed in Fig. 4, where the distributions of capillary pressure associated with the gas-phase velocity resulting from both modeling approaches are presented.

Regarding the numerical implementation of the model, it should be noted that the simulations carried out with the hydrophobic Leverett J-function often diverged in the first few hundred iterations. Although several strategies were developed to increase the stability of the numerical method, they proved insufficient to establish a robust model that worked for a wide range of operating conditions. These numerical difficulties also evidence that the hydrophobic Leverett J-function may provide an inadequate physical description of capillary transport phenomena in the anode of a DMFC. Interestingly enough, all the problems disappeared when GDL-specific drainage data were employed.

3.2. Inhomogeneous compression and liquid/gas saturation

Another aspect that deserves further attention is the dependence of the capillary pressure on liquid/gas saturation. Even though the conservation equation for the liquid saturation (derived from the mass conservation equation of the gas phase) is quite complex,

$$\nabla \cdot \left[\underbrace{\frac{\rho_g k_{rg} \bar{K}}{\mu_g}}_{\bar{\Lambda}} \left(\underbrace{\frac{\partial p_c}{\partial s} \nabla s}_{\Pi_s} + \underbrace{\frac{\partial p_c}{\partial r_p^{-1}} \nabla r_p^{-1}}_{\Pi_r} + \underbrace{\nabla p_l}_{\Pi_l} \right) \right] = \underbrace{M_m \dot{R}_m + M_w \dot{R}_w}_{\Omega}, \quad (\text{A.4})$$

for the following qualitative discussion this equation may be simplified by dropping some terms that are typically small. In particular, the source term representing the phase change rate of methanol and water, Ω , and the term associated with the pressure gradient of the liquid phase, $\nabla \cdot (\bar{\Lambda} \Pi_l)$, can be neglected in most operating conditions. This can be checked by comparing the order of magnitude of these terms to that of the capillary diffusion term associated with the liquid saturation gradient, which shall be denoted by Θ to abbreviate the formulation:

$$\nabla \cdot (\bar{\Lambda} \Pi_s) \sim \frac{\rho_g k_{rg} K_{avg} \Delta s}{\mu_g \delta_{agdl}^2} \frac{\partial p_c}{\partial s} = \Theta \quad (19)$$

Thus, straightforward order-of-magnitude estimates lead to:

$$\frac{\nabla \cdot (\bar{\Lambda} \Pi_l)}{\nabla \cdot (\bar{\Lambda} \Pi_s)} \sim \frac{\rho_g \mu_l k_{rg} |\mathbf{u}_l|}{\mu_g k_{rl} \delta_{agdl}} \frac{1}{\Theta} \sim \mathcal{O}(10^{-4}/10^{-3}) \quad (20)$$

$$\frac{\Omega}{\nabla \cdot (\bar{\Lambda} \Pi_s)} \sim \left(M_{w/m} \dot{R}_{w/m} \right) \frac{1}{\Theta} \sim \mathcal{O}(10^{-2}/10^{-1}) \quad (21)$$

On the other hand, the term associated with the gradient of the inverse of the pore radius, $\nabla \cdot (\bar{\Lambda} \Pi_r)$, is of the same order that the

capillary diffusion term associated with the liquid saturation gradient:

$$\frac{\nabla \cdot (\bar{\Lambda} \Pi_r)}{\nabla \cdot (\bar{\Lambda} \Pi_s)} \sim \frac{\rho_g k_{rg} K_{avg} \Delta r_p^{-1}}{\mu_g \delta_{agdl}^2} \frac{\partial p_c}{\partial r_p^{-1}} \frac{1}{\Theta} \sim \mathcal{O}(1) \quad (22)$$

These estimations were carried out under the same assumptions stated above for the analysis of the pressure gradient of the gas phase, ∇p_g . However, in this case there are some additional variables. The partial derivatives of the capillary pressure were calculated from Eq. (10) considering a liquid saturation level $s = 0.75$ and a porosity $\varepsilon = 0.74$. The phase change rate of methanol (m) and water (w), $\dot{R}_{w/m}$, as well as the variation of the liquid saturation, Δs , were directly estimated from the numerical results. They are typically $\mathcal{O}(1/10)$ mol/(m³·s) and $\mathcal{O}(10^{-2})$, respectively. Finally, the variation of the inverse of the pore radius, Δr_p^{-1} , was estimated in the order of $10^5/10^6$ m⁻¹.

According to the above estimations, Eq. (A.4) may be simplified, in first approximation, to:

$$\nabla \cdot \left[\frac{\rho_g k_{rg} \bar{K}}{\mu_g} \left(\frac{\partial p_c}{\partial s} \nabla s + \frac{\partial p_c}{\partial r_p^{-1}} \nabla r_p^{-1} \right) \right] = 0. \quad (23)$$

Since the inverse of the pore radius, r_p^{-1} , is a function of porosity, ε , we shall alternatively rewrite the above equation in terms of ε , instead of r_p^{-1} . Note that this change of variable is more meaningful for interpretation purposes, because saturation and porosity are both dimensionless variables, and of the same order of magnitude, so that $\mathcal{O}(|\nabla s|) \sim \mathcal{O}(|\nabla \varepsilon|)$. In addition, we shall define the ratio Γ between the partial derivative of the capillary pressure with respect to porosity, ε , and with respect to liquid saturation, s , i.e.,

$$\Gamma = \left(\frac{\partial p_c}{\partial \varepsilon} \right) / \left(\frac{\partial p_c}{\partial s} \right), \quad (24)$$

which is in turn a function of ε and s . Then, introducing the porosity in Eq. (23) and considering the above definition of Γ , we rewrite the equation in the abbreviated form:

$$\nabla \cdot [\bar{\mathbf{D}}_c (\nabla s + \Gamma \nabla \varepsilon)] = 0 \quad (25)$$

where $\bar{\mathbf{D}}_c = -(\rho_g k_{rg} / \mu_g) (\partial p_c / \partial s) \bar{\mathbf{K}}$ is the so-called capillary diffusivity tensor. Note that all the terms in this tensor are positive since capillary pressure decreases with increasing liquid saturation, i.e., $(\partial p_c / \partial s) < 0$, both for the hydrophobic Leverett J-function and the GDL-specific drainage data shown in Fig. 2.

It is interesting to note that the term associated with the porosity gradient, $R_c = \nabla \cdot (\bar{\mathbf{D}}_c \Gamma \nabla \varepsilon)$, can alternatively be written as a resistance source term affecting liquid/gas capillary transport:

$$\nabla \cdot (\bar{\mathbf{D}}_c \nabla s) + R_c = 0 \quad (26)$$

This term, associated with inhomogeneous compression effects ($\nabla \varepsilon \neq 0$), vanishes for the GDLs with uniform porosity ($\nabla \varepsilon = 0$) considered in all previous DMFC models accounting for multiphase transport effects. Due to its novelty, we shall discuss in detail the qualitative effect of this term in the description of multiphase capillary transport in the anode GDL of a DMFC.

First of all, it should be noted that if $\Gamma \ll 1$ the capillary resistance R_c is small and can be neglected, so that the inhomogeneities caused by the assembly compression of the GDL do not influence diffusive capillary transport. By way of contrast, if $\Gamma \sim 1$ the effect of the capillary resistance R_c becomes important, and it significantly affects the distribution of liquid/gas saturation. In this case, rough order-of-magnitude estimates for the two terms appearing in

Eq. (25) provides the following relation between spatial variations of saturation and porosity:

$$\nabla s \approx -\Gamma \nabla \epsilon \rightarrow \frac{\Delta s}{\Delta \epsilon} \sim -\Gamma \quad (27)$$

where Δ denotes spatial variations. Roughly speaking, the role of the capillary resistance R_c is to induce spatial variations in the saturation level that compensate the variations in capillary pressure imposed by the inhomogeneous compression (i.e., porosity gradients). As can be inferred from Eq. (27), an important aspect in the relation between the liquid saturation gradient, ∇s , and the porosity gradient, $\nabla \epsilon$, is the sign of Γ . Both the hydrophobic Leverett J-function and GDL-specific drainage data exhibit the same dependence on liquid/gas saturation, so that $(\partial p_c / \partial s)$ has the same sign in both cases. However, as previously discussed, the dependence on porosity is the opposite. Whereas the hydrophobic Leverett J-function predicts lower (i.e., more negative) capillary pressures as the GDL is compressed, GDL-specific drainage data predict higher (i.e., more positive) capillary pressures. Thus, the sign of Γ obtained in both approaches is different:

$$\text{Leverett} : \frac{\partial p_c}{\partial s} < 0, \frac{\partial p_c}{\partial \epsilon} > 0 \rightarrow \Gamma < 0 \quad (28)$$

$$\text{Drainage} : \frac{\partial p_c}{\partial s} < 0, \frac{\partial p_c}{\partial \epsilon} < 0 \rightarrow \Gamma > 0$$

Using these results in Eq. (27), it can be concluded that in the case of the hydrophobic Leverett J-function the capillary resistance R_c tends to decrease the liquid saturation level (i.e., increase the gas saturation level) in the regions where the porosity is lower, while the opposite situation results for GDL-specific drainage data. This behavior implies that R_c acts effectively as a resistance to liquid-phase capillary transport for the hydrophobic Leverett J-function, whereas it acts as a resistance to gas-phase capillary transport for GDL-specific drainage data. Considering the different signs of Γ associated with both modeling approaches, Eq. (27) leads to the following relations:

$$\text{Leverett} : \Gamma < 0 \rightarrow \frac{\Delta s}{\Delta \epsilon} > 0, \quad \text{or} \quad \frac{\Delta(1-s)}{\Delta \epsilon} < 0 \quad (29)$$

$$\text{Drainage} : \Gamma > 0 \rightarrow \frac{\Delta s}{\Delta \epsilon} < 0, \quad \text{or} \quad \frac{\Delta(1-s)}{\Delta \epsilon} > 0$$

Thus, the main effect of GDL compression (i.e., lower porosity) on the capillary transport in the anode of a DMFC can be summarized as:

$$\begin{aligned} \text{Leverett} : \downarrow \epsilon \rightarrow \downarrow s \rightarrow R_c \text{ hinders liquid transport} \\ \text{Drainage} : \downarrow \epsilon \rightarrow \downarrow 1-s \rightarrow R_c \text{ hinders gas transport} \end{aligned} \quad (30)$$

This situation is reflected by the gas saturation distribution shown in Fig. 4 for the hydrophobic Leverett J-function approach. It can be seen that the gas-void fraction is higher in the more compressed region under the rib due to the effect of the capillary resistance R_c , which hinders liquid-phase capillary transport where the porosity is lower. In contrast, the influence of the capillary resistance R_c cannot be appreciated for GDL-specific drainage data. This is due to the particular dependence that the experimental drainage curves exhibit on saturation and compression (i.e., porosity), which for the low gas-coverage factor at the GDL/Channel interface considered in the simulations of Fig. 4, $1-s^{\text{in}} = 0.05$, results in values of $\Gamma \ll 1$. A detailed discussion of the influence of the gas coverage factor is given in the following section.

As a final remark, it should be noted that the unrealistic behavior of the hydrophobic Leverett J-function discussed in the previous section has not been observed in preceding modeling studies [3,82,86,87], or even in the simulations performed herein to validate the model on an uncompressed GDL geometry. This is

because when porosity variations are ignored, $R_c = 0$, capillary transport depends only on saturation. In this situation, the gas-void fraction distribution is exclusively dominated by the effect of the capillary diffusivity \bar{D}_c . In consequence, a higher gas saturation level results under the rib due to the larger capillary diffusion path (see Fig. 3). This, in turn, leads to higher (less negative) capillary pressures in the region under the rib and, therefore, a realistic gas-flow towards the channel. The potential effect of the inhomogeneous compression cannot be appreciated.

Note also that, in the absence of inhomogeneous compression effects, both the hydrophobic Leverett J-function and GDL-specific drainage data predict a similar behavior. The reason is that both modeling approaches present the same dependence on saturation (capillary pressure decreases with s) and thus the capillary diffusivity, $\bar{D}_c (\propto \partial p_c / \partial s)$, has the same sign. The only difference between them is that the pressure of the liquid phase is higher than the pressure of the gas phase for the hydrophobic Leverett J-function approach ($p_c = p_g - p_l < 0$), while the situation is the opposite for GDL-specific drainage data ($p_c = p_g - p_l > 0$).

3.3. Influence of the gas coverage factor at the GDL/Channel interface

As previously discussed, the capillary resistance, $R_c = \nabla \cdot (\bar{D}_c \Gamma \nabla \epsilon)$, plays a key role in determining the liquid/gas saturation distribution in the presence of inhomogeneous compression effects. However, the relative importance of the capillary resistance and capillary diffusion terms in Eq. (26) depends largely on the gas coverage factor at the GDL/Channel interface, $1-s^{\text{in}}$. Indeed, the above expression for R_c shows that the variable that governs the gas-void fraction distribution is the ratio Γ , which is in turn a function of the porosity, ϵ , and the gas saturation level, $1-s$.

Focusing hereafter our attention on empirical GDL-specific drainage data, Fig. 5 shows that the influence of the capillary resistance R_c results negligible, $\Gamma \ll 1$, when the gas saturation is close to zero or approximates the value of the residual liquid saturation, $1-s_r \approx 0.9$. In contrast, the effect of the capillary resistance R_c becomes important, $\Gamma \sim \mathcal{O}(1)$, for intermediate gas saturations. This behavior is a consequence of the shape of the p_c-s curves associated with GDL-specific data. As can be seen in Fig. 2, the slope of the empirical drainage curves significantly increases when the liquid saturation is near zero or close to its residual value, $s_r \approx 0.1$. However, it presents moderate values for intermediate

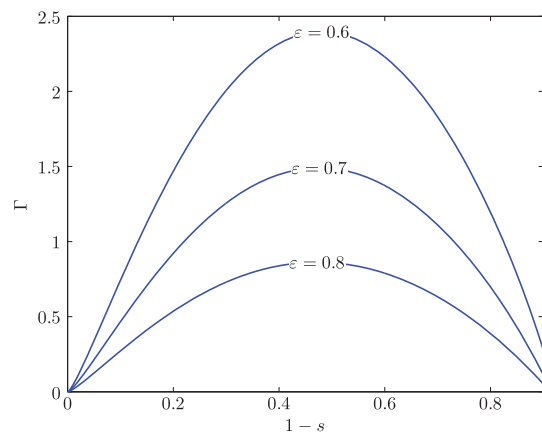


Fig. 5. Variation of $\Gamma = (\partial p_c / \partial \epsilon) / (\partial p_c / \partial s)$ with the gas-void fraction, $1-s$, obtained from GDL-specific drainage data [74]. The different curves correspond to different values of the porosity, ϵ .

saturations. Note also that the ratio Γ increases with decreasing porosity. It should be pointed out that this behavior is not appreciated on the hydrophobic Leverett J-function approach. In this case, the capillary resistance R_c is always comparable to the capillary diffusion term, $\nabla \cdot (-\mathbf{D}_c \nabla s)$, so that $\Gamma \sim \mathcal{O}(1)$ regardless of the value of s .

The situation discussed above is illustrated in Fig. 6. This figure shows the gas-void fraction distributions obtained for three different gas coverage factors at the GDL/Channel interface ($1 - s^{\text{in}} = 0, 0.2, 0.4$) on a 20% compressed GDL. Note that these gas coverage factors are in the range of those obtained numerically by Yang et al. [82]. It can be seen that for small channel gas-void fractions ($1 - s^{\text{in}} \rightarrow 0$) the influence of the capillary resistance R_c turns out to be negligible. In this case, the gas saturation distribution is exclusively dominated by the effect of the capillary diffusivity \mathbf{D}_c . Accordingly, higher gas-void fractions are found under the rib due to the larger capillary diffusion path. This type of solution is similar to those previously presented in this study (see, e.g., Figs. 3 and 4) and in the literature [3,82,86,87]. By way of contrast, the effect of the capillary resistance R_c becomes important as soon as the gas saturation level becomes larger. As previously discussed, when GDL-specific drainage data are considered the capillary resistance R_c hinders gas capillary transport in the regions where the porosity decreases, so that lower gas-void fractions are found under the rib. In particular, the gas-void fraction decreases significantly under the rib corner due to the sharp reduction of the pore size there. The strong gas-void fraction gradients established in this singular region may indicate a preferential location for the evacuation of gas-phase bubbles from the GDL to the channel, consistent with the in-situ observations made by Hartnig et al. [90] in an operating DMFC by means of X-ray synchrotron radiography.

The effect induced by the inhomogeneous compression on the gas-void fraction distribution is physically sound. It should be expected that the regions with larger pores (i.e., higher porosity) trap more gas. Furthermore, this result agrees with other PEMFC modeling studies focused on the influence of GDL spatially-varying properties on two-phase transport phenomena [24,25]. These

works concluded that the spatial variations induced by the inhomogeneities of the GDL (PTFE treatment, manufacturing process and assembly compression) may justify the spatial patterns observed experimentally in the water distribution throughout the GDL. However, the effect induced by the capillary resistance R_c in a PEMFC is the opposite to that observed here for the anode of a DMFC. In fact, these works employed the hydrophobic Leverett J-function which seems to be more appropriate to describe capillary transport under the two-phase flow conditions present in PEMFCs. As a result, the capillary resistance R_c hinders liquid capillary transport, and more liquid water is trapped in the regions with larger pores (i.e., higher porosity).

From the experimental point of view, the potential effect of GDL inhomogeneous compression on capillary transport has been explored in a few works related with PEMFCs. It is worth mentioning the ex-situ experimental works carried out by Bazylak et al. [91] and Gao et al. [92] by means of fluorescence microscopy and neutron radiography, respectively. Even though both works showed that the inhomogeneous compression has a significant impact on the water distribution level in the GDL (Toray[®] carbon paper TGP-H series, 10% wet-proof), opposite conclusions were derived from them. Bazylak et al. [91] found that the compressed regions of the GDL provided preferential pathways for water transport and breakthrough. This behavior was attributed to the irreversible damage of the PTFE coating and fibers in the compressed regions, a physical mechanism that is not reproduced in our model. In contrast, Gao et al. [92] showed that the liquid water saturation level under the ribs was less than that under the channels both before and after the breakthrough event. This phenomenon was attributed to the changes in the morphological properties induced by the compression, lower void volume and smaller pore sizes. This contradictory situation evidences that the influence of compression on capillary transport should be further analyzed in future work.

According to the investigation carried out here, the different results presented in these studies may be explained qualitatively by the different signs of the relevant Gamma parameter associated with the tested GDLs as they were compressed. In Ref. [91] the excessive damage of the PTFE content under the rib seems to dominate over the pore size reduction caused by the GDL compression. Therefore, the relevant Gamma parameter would be that associated with PTFE content, i.e., the ratio between the partial derivative of the capillary pressure with respect to PTFE content and with respect to liquid saturation. This ratio is positive, since a lower PTFE content displaces the $p_c - s$ imbibition curves, which are those of interest to describe the invasion process of water into the air-filled GDL, to higher (i.e., less negative) capillary pressures [75]. Thus, the effect of reducing the PTFE content of the GDL on the experimental imbibition $p_c - s$ curves is qualitatively the opposite to that of reducing the porosity (i.e., increasing the compression ratio) of the GDL according to the capillary pressure measurements carried out by Gostick et al. [74,75] which were considered in this work. Accordingly, more water should be expected under the rib due to the capillary resistance R_c induced by the higher PTFE content under the channel.

By way of contrast, Gao et al. [92] attributed the higher water saturation observed under the channel to the changes in the morphological properties of the GDL induced by compression, lower void volume and smaller pore sizes. In this case the experimental observations are consistent with the capillary pressure measurements considered here [74,75]. The relevant Gamma parameter would be that associated with the changes in porosity (pore size), as defined in Eq. (24). And consequently, the negative value of Gamma corresponding to the experimental imbibition curves will lead to a lower liquid saturation level under the rib. Thus, more water should be expected under the channel where the pore sizes are larger.

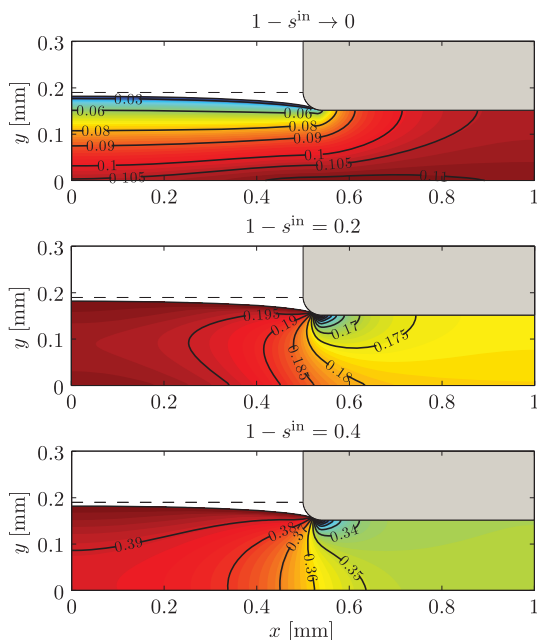


Fig. 6. Gas-void fraction, $1-s$, for different gas coverage factors at the GDL/Channel interface, $1-s^{\text{in}}$. Operating conditions: $V = 0.2$ V, CR = 20%, $C_{\text{ml}}^{\text{in}} = 1$ M, $T = 80$ °C.

4. Conclusions

An isothermal two-phase 2D/1D model for the anode of a liquid-feed DMFC is presented. The model takes into account the effects of the inhomogeneous assembly compression of the GDL, incorporated through the non-uniform porosity distribution provided by a previous analysis of the GDL compression process [11]. The effective anisotropic properties of the GDL (i.e., diffusivity, permeability, and electrical conductivity) are correlated as a function of porosity through experimental data reported in the literature corresponding to Toray® carbon paper TGP-H series. While a growing consensus was found for dry effective properties, extensive experimental and numerical work is still needed to characterize two-phase properties. The model also incorporates experimental capillary pressure curves reflecting the mixed-wettability characteristics of GDLs, as a major improvement with respect to the traditional Leverett J-function approach. Due to the uncertainty in the experimental characterization of the $p_c - s$ curves of CLs, the model assumes a constant saturation profile at the GDL/CL interface. This capillary boundary condition, although inconsistent with physical nature, is not expected to affect the main results of this paper, concerned with the effects of the inhomogeneous assembly compression on the two-phase transport phenomena in the anode GDL of a DMFC.

Focusing on the numerical results, it is shown that the inhomogeneous compression of the GDL has a large impact on two-phase transport phenomena in this key element of the cell. The numerical results evidence that the hydrophobic Leverett J-function approach ($\theta_c > 90^\circ$) traditionally employed in DMFC modeling studies is physically inconsistent to describe capillary transport in the anode of a DMFC. In contrast, more realistic results are obtained when GDL-specific drainage data (gas-phase displaces liquid-phase) are taken into account. Moreover, it is found that the gas saturation distribution in the GDL can be characterized by the ratio Γ , which measures the relative influence of the capillary resistance induced by the inhomogeneous compression, $R_c (\propto \partial p_c / \partial \epsilon)$, to the well established capillary diffusivity, $\bar{D}_c (\propto \partial p_c / \partial s)$. For small gas-void fractions Γ is also small, and the capillary diffusivity is the dominant two-phase transport mechanism, so that the gas saturation level is higher under the rib due to the larger capillary diffusion path. On the other hand, for larger gas-void fractions Γ is of order unity, and the effect of the capillary resistance R_c becomes important, leading to higher gas-void fractions in the region under the channel due to the larger pore sizes there.

A few ex-situ experimental works exploring the influence of GDL inhomogeneous compression on capillary water transport and breakthrough were found in the literature; however, opposite conclusions were derived from them. Thus, further studies on the effect of GDL compression on two-phase capillary transport are warranted. These works would surely benefit from the introduction of generalized Γ ratios, such as the one defined here, to characterize the influence of inhomogeneous operating conditions (temperature, methanol concentration, etc.) and GDL properties (pore size, interfacial contact angle, etc.) on capillary transport phenomena. Experiments reporting the invasion process of gaseous carbon dioxide in saturated and partially saturated GDLs with methanol aqueous solutions, more relevant for the two-phase conditions present in the anode of a DMFC, would be of particular interest to validate the numerical findings presented here.

As a final remark, it is worth noting that the present 2D across-the-channel constitutes only a first step towards the development of a full 3D-model for DMFCs that takes into account the influence of inhomogeneous compression effects on multiphase transport phenomena. Therefore, further work is still required to implement the 3D-model and to validate its results by direct comparison with experimentally observed quantities.

Acknowledgments

This work was supported by Project ENE2011-24574 of the Spanish Ministerio de Economía y Competitividad. The authors thank Dr. Jeff Gostick (McGill University) for fruitful discussions and comments concerning this work.

Appendix A. Model formulation

A.1. 2D model (anode GDL)

In the following sections, bold symbols denote two-dimensional vectors, e.g., $\mathbf{u}_i = (u_{ix}, u_{iy})$, and overlined bold symbols denote two-dimensional orthotropic tensors, e.g.,

$$\bar{\mathbf{K}} = \begin{bmatrix} K_{xx} & 0 \\ 0 & K_{yy} \end{bmatrix} = \begin{bmatrix} K^{ip} & 0 \\ 0 & K^{tp} \end{bmatrix} \quad (\text{A.1})$$

A.1.1. Conservation equations

$$\nabla \cdot (\rho_l \mathbf{u}_l) = -M_m \dot{R}_m - M_w \dot{R}_w \quad (\text{A.2})$$

$$\mathbf{u}_l = -\frac{k_{dl}}{\mu_l} \bar{\mathbf{K}} \nabla p_l \quad (\text{A.3})$$

$$\nabla \cdot \left[-\frac{\rho_g k_{rg}}{\mu_g} \bar{\mathbf{K}} \left(\frac{\partial p_c}{\partial s} \nabla s + \frac{\partial p_c}{\partial r_p^{-1}} \nabla r_p^{-1} + \nabla p_l \right) \right]$$

$$= M_m \dot{R}_m + M_w \dot{R}_w \quad (\text{A.4})$$

$$\mathbf{u}_g = -\frac{k_{rg}}{\mu_g} \bar{\mathbf{K}} \nabla p_g \quad (\text{A.5})$$

$$\nabla \cdot (\mathbf{u}_l C_{ml}) - \nabla \cdot (\bar{\mathbf{D}}_{ml,l}^{\text{eff}} \nabla C_{ml}) = -\dot{R}_m \quad (\text{A.6})$$

$$\nabla \cdot (\mathbf{u}_g C_{mv}) - \nabla \cdot \left[\rho_g \bar{\mathbf{D}}_{mv,g}^{\text{eff}} \nabla \left(\frac{C_{mv}}{\rho_g} \right) \right] = \dot{R}_m \quad (\text{A.7})$$

$$\nabla \cdot (\mathbf{u}_g C_{wv}) - \nabla \cdot \left[\rho_g \bar{\mathbf{D}}_{wv,g}^{\text{eff}} \nabla \left(\frac{C_{wv}}{\rho_g} \right) \right] = \dot{R}_w \quad (\text{A.8})$$

$$\nabla \cdot (\bar{\sigma}^{\text{eff}} \nabla \phi) = 0 \quad (\text{A.9})$$

A.1.2. Boundary conditions

GDL/Channel interface (thermodynamic equilibrium):

$$p_l = p_l^{\text{in}}, \quad s = s^{\text{in}}, \quad C_{ml} = C_{ml}^{\text{in}}, \quad C_{mv} = C_{mv}^{\text{sat}}, \quad C_{wv} = C_{wv}^{\text{sat}}, \quad (\bar{\sigma}^{\text{eff}} \nabla \phi) \cdot \mathbf{n} = 0 \quad (\text{A.10})$$

GDL/Rib interface:

$$\mathbf{u}_l \cdot \mathbf{n} = 0 \quad (\text{A.11a})$$

$$\left[-\frac{\rho_g k_{rg}}{\mu_g} \bar{\mathbf{K}} \left(\frac{\partial p_c}{\partial s} \nabla s + \frac{\partial p_c}{\partial r_p^{-1}} \nabla r_p^{-1} + \nabla p_l \right) \right] \cdot \mathbf{n} = 0 \quad (\text{A.11b})$$

$$(\mathbf{u}_l C_{ml} - \bar{\mathbf{D}}_{ml,l}^{\text{eff}} \nabla C_{ml}) \cdot \mathbf{n} = 0 \quad (\text{A.11c})$$

$$\left[\mathbf{u}_g C_{mv} - \rho_g \bar{\mathbf{D}}_{mv,g}^{\text{eff}} \nabla \left(\frac{C_{mv}}{\rho_g} \right) \right] \cdot \mathbf{n} = 0 \quad (\text{A.11d})$$

$$\left[\mathbf{u}_g C_{wv} - \rho_g \bar{\mathbf{D}}_{wv,g}^{\text{eff}} \nabla \left(\frac{C_{wv}}{\rho_g} \right) \right] \cdot \mathbf{n} = 0 \quad (\text{A.11e})$$

$$\phi = \phi_{\text{rib}} \quad (\text{A.11f})$$

GDL/CL interface:

$$(\rho_l \mathbf{u}_l) \cdot \mathbf{n} = M_w (N_{wl} + \dot{R}_{w,\text{acl}} \delta_{\text{acl}}) + M_m (N_{ml} + \dot{R}_{m,\text{acl}} \delta_{\text{acl}}) \quad (\text{A.12a})$$

$$\left[-\frac{\rho_g k_{rg}}{\mu_g} \bar{\mathbf{K}} \left(\frac{\partial p_c}{\partial s} \nabla s + \frac{\partial p_c}{\partial r_p^{-1}} \nabla r_p^{-1} + \nabla p_l \right) \right] \cdot \mathbf{n} = -M_w \dot{R}_{w,\text{acl}} \delta_{\text{acl}} - M_m \dot{R}_{m,\text{acl}} \delta_{\text{acl}} - M_{\text{CO}_2} N_{\text{CO}_2} \quad (\text{A.12b})$$

$$(\mathbf{u}_l C_{ml} - \bar{\mathbf{D}}_{ml,l}^{\text{eff}} \nabla C_{ml}) \cdot \mathbf{n} = N_{ml} + \dot{R}_{m,\text{acl}} \delta_{\text{acl}} \quad (\text{A.12c})$$

$$\left[\mathbf{u}_g C_{mv} - \rho_g \bar{\mathbf{D}}_{mv,g}^{\text{eff}} \nabla \left(\frac{C_{mv}}{\rho_g} \right) \right] \cdot \mathbf{n} = -\dot{R}_{m,\text{acl}} \delta_{\text{acl}} \quad (\text{A.12d})$$

$$\left[\mathbf{u}_g C_{wv} - \rho_g \bar{\mathbf{D}}_{wv,g}^{\text{eff}} \nabla \left(\frac{C_{wv}}{\rho_g} \right) \right] \cdot \mathbf{n} = -\dot{R}_{w,\text{acl}} \delta_{\text{acl}} \quad (\text{A.12e})$$

$$(-\bar{\sigma}^{\text{eff}} \nabla \phi) \cdot \mathbf{n} = -i \quad (\text{A.12f})$$

A.2. 1D model (CLs, membrane, and cathode GDL)

At the GDL/CL interface the 2D model is locally coupled to a 1D model accounting for the electrochemical reactions in both the anode and the cathode, as well as the mixed potential associated with methanol crossover. The output variables provided by the 1D model at each computational face along the GDL/CL interface are the current density, i , the molar flux of liquid water, N_{wl} , the molar flux of liquid methanol, N_{ml} , and the molar flux of carbon dioxide, N_{CO_2} . The model assumes non-Tafel kinetics to describe the complex kinetics of the multi-step Methanol Oxidation Reaction (MOR) and first-order Tafel-like kinetics to model the Oxygen Reduction Reaction (ORR) [6]. The dissolving process of oxygen in the triple boundary points where the reaction takes place is incorporated through the Henry constant k_{H,O_2} . To describe the methanol-crossover flux across the membrane, N_{cross} , both diffusive transport and electro-osmotic drag phenomena are taken into account. Finally, the diffusive mass transport of oxygen at the cathode GDL is modeled by considering a single-phase Bruggeman-type resistance. The equations describing the 1D model are as follows:

$$i + 6FN_{\text{cross}} = \delta_{\text{ccl}}(ai_0)_c \left(\frac{C_{\text{O}_2,\text{ccl}}}{k_{\text{H},\text{O}_2} C_{\text{O}_2,\text{ref}}} \right) \exp \left(\frac{\alpha_c F}{RT} \eta_c \right) \quad (\text{A.13a})$$

$$i = \delta_{\text{acl}}(ai_0)_a \frac{\kappa C_{\text{ml},\text{acl}} \exp \left(\frac{\alpha_a F}{RT} \eta_a \right)}{C_{\text{ml},\text{acl}} + \lambda \exp \left(\frac{\alpha_a F}{RT} \eta_a \right)} \quad (\text{A.13b})$$

$$N_{\text{O}_2} = \frac{i}{4F} + \frac{3}{2} N_{\text{cross}} = \frac{D_{\text{O}_2}^{\text{eff}}}{\delta_{\text{cgl}}} (C_{\text{O}_2,\text{amb}} - C_{\text{O}_2,\text{ccl}}) \quad (\text{A.13c})$$

$$N_{\text{cross}} = n_d^m \frac{i}{F} + \frac{D_{m,\text{mem}}^{\text{eff}}}{\delta_{\text{mem}}} C_{\text{ml},\text{acl}}; \quad n_d^m = \frac{M_w}{\rho_w} n_d^w C_{\text{ml},\text{acl}} \quad (\text{A.13d})$$

$$N_{\text{ml}} = \frac{i}{6F} + N_{\text{cross}} \quad (\text{A.13e})$$

$$N_{wl} = \left(\frac{1}{6} + n_d^w \right) \frac{i}{F} \quad (\text{A.13f})$$

$$N_{\text{CO}_2} = \frac{i}{6F} \quad (\text{A.13g})$$

The solution of the system of Eqs. (A.13a)–(A.13d) provides expressions for the anode and cathode overpotentials, η_a and η_c , respectively, as a function of the local current density, i , and the liquid methanol concentration at the anode catalyst layer, $C_{\text{ml},\text{acl}}$. Introducing the resulting expressions in the equation for the cell voltage, V_{cell} , we obtain the following nonlinear relation among i , $C_{\text{ml},\text{acl}}$, ϕ_{acl} and V_{cell} :

$$f(i, C_{\text{ml},\text{acl}}, \phi_{\text{acl}}) \equiv E_{\text{cell}} - V_{\text{cell}} - \eta_a(i, C_{\text{ml},\text{acl}}) - \eta_c(i, C_{\text{ml},\text{acl}}) - i \left(\frac{\delta_{\text{mem}}}{\sigma_{\text{mem}}} \right) - 2(\phi_{\text{acl}} - \phi_{\text{rib}}) = 0 \quad (\text{A.14})$$

In this expression E_{cell} is the ideal thermodynamic cell voltage, and the terms $i(\delta_{\text{mem}}/\sigma_{\text{mem}})$ and $2(\phi_{\text{acl}} - \phi_{\text{rib}})$ represent the ohmic losses across the polymer membrane and the GDLs, respectively. Note that the voltage drop across the GDL is assumed equal for both electrodes. In addition, the almost equipotential surface of the anode rib is considered as the reference electronic potential; see boundary condition (A.11f).

The solution of Eq. (A.14) determines the local current density i at each face along the GDL/CL interface, for given local values of $C_{\text{ml},\text{acl}}$ and ϕ_{acl} coming from the solution of the 2D model at every iteration and for a given fixed value of V_{cell} . Along with expressions (A.13d)–(A.13g), this links the 2D and 1D models through boundary conditions (A.12a)–(A.12c) and (A.12f), thus closing the mathematical problem.

Nomenclature

Symbols

A_{lg}	specific liquid/gas interfacial area [m^{-1}]
a	catalyst surface area per unit volume [m^{-1}]
C	molar concentration [mol m^{-3}]
CR	thickness compression ratio; see Eq. (12)
$\bar{\mathbf{D}}_c$	capillary diffusivity tensor; see Eq. (25) [$\text{Kg m}^{-1} \text{s}^{-1}$]
E_{cell}	ideal thermodynamic cell voltage [V]
F	Faraday's constant [C mol^{-1}]
$f(\varepsilon)$	normalized porosity function; see Eq. (1)
$g(s)$	normalized saturation function; see Eq. (1)
h_{lg}	liquid/gas mass transfer coefficient [m s^{-1}]
i	current density [A m^{-2}]
i_0	exchange current density [A m^{-2}]
$J(s)$	Leverett J-function; see Eq. (8)
$\bar{\mathbf{K}}$	absolute permeability tensor [m^2]
k_{H}	Henry's law constant (methanol [Pa], oxygen [-])
k_{evp}	evaporation rate constant [Pa s^{-1}]
k_{con}	condensation rate constant [s^{-1}]
k_r	relative permeability
M	molecular weight [kg mol^{-1}]
m	Van Genuchten constant; see Eq. (9)
N	molar flux [$\text{mol m}^{-2} \text{s}^{-1}$]

n	Van Genuchten constant; see Eq. (9)
\mathbf{n}	outward normal unit vector
n_d^i	electro-osmotic drag coefficient of species i
p	static pressure [Pa]
p_c	capillary pressure, defined as $p_c = p_g - p_l$ [Pa]
$p_{c,b}$	Van Genuchten constant; see Eq. (9) [Pa]
R	universal gas constant [$\text{J mol}^{-1} \text{K}^{-1}$]
R_c	capillary resistance defined in Eq. (26) [$\text{Kg m}^{-3} \text{s}^{-1}$]
\dot{R}	interfacial mass transfer rate [$\text{mol m}^{-3} \text{s}^{-1}$]
r	fillet radius [m]
r_p	characteristic pore radius; see Eq. (11) [m]
s	liquid saturation
s_r	residual liquid saturation; see Eq. (9)
$1-s$	gas saturation
T	temperature [K]
\mathbf{u}	(superficial) velocity vector [m s^{-1}]
V_{cell}	output cell voltage [V]
w	half-width [m]
X_i	mole fraction of species i
x	in-plane coordinate [m]
y	through-plane coordinate [m]

Greek letters

α	transfer coefficient
β	interpolation parameter defined in Eq. (10)
Γ	ratio defined in Eq. (24)
δ	thickness [m]
ε	porosity
η	overpotential [V]
κ	experimental constant
θ_c	contact angle [$^\circ$]
λ	experimental constant [mol m^{-3}]
μ	dynamic viscosity [$\text{kg m}^{-1} \text{s}^{-1}$]
ρ	density [kg m^{-3}]
σ	interfacial tension [N m^{-1}]; proton conductivity [S m^{-1}]
$\bar{\sigma}$	electrical conductivity tensor [S m^{-1}]
φ	electronic potential [V]

Subscripts

a	anode
acl	anode catalyst layer
agdl	anode gas diffusion layer
amb	ambient
avg	average value
c	cathode
ccl	cathode catalyst layer
cgdl	cathode gas diffusion layer
cross	crossover
g	gas phase
i	species i
j	phase j ($=l/g$, or liquid/gas phase)
l	liquid phase
m	methanol
mem	membrane
mv	methanol vapor
ref	reference value
rib	bipolar plate rib
w	water
wv	water vapor

Superscripts

bulk	bulk property
c	compressed

dry	single-phase conditions
eff	effective
in	inlet condition at the GDL/Channel interface
ip	in-plane direction
sat	saturated conditions
tp	through-plane direction
u	uncompressed
wet	multiphase flow conditions

Table A.1

Physical constants, transport, kinetic and design parameters.

Parameter	Value	Reference
F	96485 C mol^{-1}	–
R	$8.314 \text{ J mol}^{-1} \text{K}^{-1}$	–
M_m	$0.032 \text{ kg mol}^{-1}$	–
M_w	$0.018 \text{ kg mol}^{-1}$	–
M_{CO_2}	$0.044 \text{ kg mol}^{-1}$	–
$X_{\text{O}_2, \text{amb}}$	0.21 (air)	–
$p_{\text{in}}^{\text{amb}}$	$1.013 \times 10^5 \text{ Pa}$	–
p_{in}^{a}	$1.013 \times 10^5 \text{ Pa}$	–
p_c	$1.013 \times 10^5 \text{ Pa}$	–
$\varepsilon_{\text{agdl}}^{\text{u}}$	0.78	[38]
ε_{acl}	0.3	[3]
$\varepsilon_{\text{cgdl}}$	0.78	[38]
μ_1	$1000 - 0.0178 (T - 277.15)^{1.7} \text{ kg m}^{-3}$	[93]
μ_l	$0.458509 - 5.30474 \times 10^{-3} T + 2.31231 \times 10^{-5} T^2 - 4.49161 \times 10^{-8} T^3 + 3.27681 \times 10^{-11} T^4 \text{ kg m}^{-1} \text{s}^{-1}$	[93]
μ_g	$2.03 \times 10^{-5} \text{ kg m}^{-1} \text{s}^{-1}$	[3]
$D_{\text{bulk}}^{\text{ml, water}}$	$10^{-5.4163 - (999.787/T)} \text{ m}^2 \text{s}^{-1}$	[94]
$D_{\text{mv, gas}}^{\text{bulk}}$	$-6.954 \times 10^{-6} + 4.5986 \times 10^{-8} T + 9.4979 \times 10^{-11} T^2 \text{ m}^2 \text{s}^{-1}$	[3]
$D_{\text{wv, gas}}^{\text{bulk}}$	$2.56 \times 10^{-5} \left(\frac{T}{307.15}\right)^{2.334} \text{ m}^2 \text{s}^{-1}$	[3]
$D_{\text{O}_2, \text{air}}^{\text{bulk}}$	$2.5 \times 10^{-5} \left(\frac{T}{298}\right)^{3/2} \left(\frac{p_{\text{amb}}}{p^0}\right) \text{ m}^2 \text{s}^{-1}$	[95]
$D_{\text{m, mem}}^{\text{eff}}$	$4.9 \times 10^{-10} \exp[2436(\frac{1}{333} - \frac{1}{T})] \text{ m}^2 \text{s}^{-1}$	[96]
n_d^{w}	$2.9 \exp[1029(\frac{1}{333} - \frac{1}{T})]$	[97]
k_{evp}	$10^{-6} \text{ Pa}^{-1} \text{s}^{-1}$	–
k_{con}	10^3 s^{-1}	–
$\log_{10}(p_{\text{wv}}^{\text{sat}})$	$-2.1794 + 0.02953 (T - 273) - 9.1837 \times 10^{-5} (T - 273)^2 + 1.4454 \times 10^{-7} (T - 273)^3 \text{ atm}$	[3]
$k_{\text{H}_2\text{O}_2}$	$\exp\left[\frac{-666/T + 14.1}{RT}\right]$	[3]
$k_{\text{H}_2\text{m}}$	$0.096 \exp[0.04511 (T - 273)] \text{ atm}$	[3]
σ_{mem}	$7.3 \exp[1268(\frac{1}{298} - \frac{1}{T})] \text{ S m}^{-1}$	[96]
a_a	10^5 m^{-1}	[98]
a_c	10^5 m^{-1}	[98]
$i_{0,a}$	$94.25 \exp[\frac{35570}{R}(\frac{1}{353} - \frac{1}{T})] \text{ A m}^{-2}$	[6]
$i_{0,c}$	$0.04222 \exp[\frac{73200}{R}(\frac{1}{353} - \frac{1}{T})] \text{ A m}^{-2}$	[1]
α_a	0.5	[84]
α_c	1	[3]
κ	7.5×10^{-4}	[98]
λ	$2.8 \times 10^{-3} \text{ mol m}^{-3}$	[98]
$C_{\text{O}_2, \text{ref}}$	0.52 mol m^{-3}	[3]
E_{cell}	$1.213 - 1.4 \times 10^{-4} (T - 298) - \frac{0.5 RT}{2 F} \log\left(\frac{p_{\text{in}}^{\text{u}}}{p_{\text{amb}}}\right) \text{ V}$	[96]

References

- [1] Z.H. Wang, C.-Y. Wang, J. Electrochem. Soc. 150 (2003) A508–A519.
- [2] K. Matsuoka, Y. Iriyama, T. Abe, M. Matsuoka, Z. Ogumi, J. Power Sources 150 (2005) 27–31.
- [3] W.-W. Yang, T.-S. Zhao, J. Power Sources 174 (2007) 136–147.
- [4] S.K. Kamarudin, F. Achmad, W.R.W. Daud, Int. J. Hydrogen Energy 34 (2009) 6902–6916.
- [5] T.-S. Zhao, C. Xu, R. Chen, W.-W. Yang, Prog. Energy Combust. 35 (2009) 275–292.
- [6] M. Vera, J. Power Sources 171 (2007) 763–777.
- [7] T. Arlt, I. Manke, K. Wippermann, H. Riesemeier, J. Mergel, J. Banhart, J. Power Sources 221 (2013) 210–216.
- [8] I. Nitta, Doctoral dissertation, Helsinki University of Technology, Finland, 2008.
- [9] L. Cindrella, A.M. Kannan, J.F. Lin, K. Saminathan, Y. Ho, C.W. Lin, J. Wertz, J. Power Sources 194 (2009) 146–160.
- [10] X. Zhang, D.-T. Song, Q.-P. Wang, C. Huang, Z.-S. Liu, ECS Trans. 16 (2008) 913–923.

- [11] P.A. García-Salaberri, M. Vera, R. Zaera, *Int. J. Hydrogen Energy* 36 (2011) 11856–11870.
- [12] J.P. James, H.-W. Choi, J.G. Pharoah, *Int. J. Hydrogen Energy* 37 (2012) 18216–18230.
- [13] I. Nitta, T. Hottinen, O. Himanen, M. Mikkola, *J. Power Sources* 171 (2007) 26–36.
- [14] T. Hottinen, O. Himanen, S. Karvonen, I. Nitta, *J. Power Sources* 171 (2007) 113–121.
- [15] I. Nitta, O. Himanen, M. Mikkola, *Fuel Cells* 08 (2008) 111–119.
- [16] C.-Y. Wang, *Chem. Rev.* 104 (2004) 4727–4766.
- [17] N. Djilali, *Energy* 32 (2007) 269–280.
- [18] A. Arvay, E. Yli-Rantala, C.-H. Liu, X.-H. Peng, P. Koski, L. Cindrella, P. Kauranen, P.M. Wilde, A.M. Kannan, *J. Power Sources* 213 (2012) 317–337.
- [19] C. Siegel, *Energy* 33 (2008) 1331–1352.
- [20] N. Zamel, X. Li, *Prog. Energ. Combust.* 39 (2013) 111–146.
- [21] P.C. Sui, N. Djilali, *J. Power Sources* 161 (2006) 294–300.
- [22] P. Zhou, C.W. Wu, *J. Power Sources* 170 (2007) 93–100.
- [23] G. He, Y. Yamazaki, A. Abudula, *J. Power Sources* 195 (2010) 1551–1560.
- [24] Y. Wang, K.S. Chen, *J. Electrochem. Soc.* 158 (2011) B1292–B1299.
- [25] K. Kang, K. Oh, S. Park, A. Jo, H. Ju, *J. Power Sources* 212 (2012) 93–99.
- [26] A. Ismail, S.K. Kamarudin, W.R.W. Daud, S. Masdar, M.R. Yosfiah, *J. Power Sources* 196 (2011) 9847–9855.
- [27] H. Bahrami, A. Faghri, *J. Power Sources* 230 (2013) 303–320.
- [28] M. Möst, M. Rzepka, U. Stimming, *J. Power Sources* 191 (2009) 456–464.
- [29] Z. Miao, Y.-L. He, J.-Q. Zou, *J. Power Sources* 195 (2010) 3693–3708.
- [30] Z. Miao, Y.-L. He, T.-S. Zhao, W.-Q. Tao, *Front. Heat Mass Transf.* 2 (2011) 013001.
- [31] Y.-L. He, Z. Miao, T.-S. Zhao, W.-W. Yang, *Int. J. Hydrogen Energy* 37 (2012) 4422–4438.
- [32] J. Ge, Doctoral dissertation, University of Miami, USA, 2005.
- [33] Y. Zhu, C. Liu, J. Liang, L. Wang, *J. Power Sources* 196 (2011) 264–269.
- [34] S.-J. Lee, C.-D. Hsu, C.-H. Huang, *J. Power Sources* 145 (2005) 353–361.
- [35] J.-H. Lin, W.-H. Chen, Y.-J. Su, T.-H. Ko, *Fuel* 87 (2008) 2420–2424.
- [36] G. Dotelli, L. Omati, P.G. Stampino, P. Grassini, D. Brivio, *J. Power Sources* 196 (2011) 8955–8966.
- [37] H.-M. Chang, M.-H. Chang, *Appl. Mech. Mater.* 110–116 (2012) 48–52.
- [38] Toray Carbon Fiber Paper “TGP-H” Datasheet, Toray Industries Inc., Advanced Composites Dept., Tokyo, 2001.
- [39] Z. Fishman, A. Bazylak, *J. Electrochem. Soc.* 158 (2011) B247–B252.
- [40] Z. Fishman, A. Bazylak, *J. Electrochem. Soc.* 158 (2011) B841–B845.
- [41] A. Rofaief, J.S. Ellis, P. Challa, A. Bazylak, *J. Power Sources* 201 (2012) 219–225.
- [42] H.-R. Jhong, F.R. Brushett, L. Yin, D.M. Stevenson, P.J.A. Kenis, *J. Electrochem. Soc.* 159 (2012) B292–B298.
- [43] C.J. Van Duijn, J. Molenaar, M.J. de Neef, *Transport Porous Med.* 21 (1995) 71–93.
- [44] A. Kusoglu, A. Kwong, K.T. Clark, H.P. Gunterman, A.Z. Weber, *J. Electrochem. Soc.* 159 (2012) F530–F535.
- [45] J.H. Nam, M. Kaviani, *Int. J. Heat Mass Tran.* 46 (2003) 4595–4611.
- [46] R. Flückiger, S.A. Freunberger, D. Kramer, A. Wokaun, G.G. Scherer, F.N. Büchi, *Electrochim. Acta* 54 (2008) 551–559.
- [47] R. Flückiger, Doctoral dissertation, ETH Zurich, Switzerland, 2009.
- [48] N. Zamel, N.G.C. Astrath, X. Li, J. Shen, J. Zhou, F.B.G. Astrath, H. Wang, Z.-S. Liu, *Chem. Eng. Sci.* 65 (2010) 931–937.
- [49] J.M. LaManna, S.G. Kandlikar, *Int. J. Hydrogen Energy* 36 (2011) 5021–5029.
- [50] N. Zamel, X. Li, J. Shen, *Energy & Fuels* 23 (2009) 6070–6078.
- [51] R. Wu, X. Zhu, Q. Liao, H. Wang, Y.-D. Ding, J. Li, D.-D. Ye, *Electrochim. Acta* 55 (2010) 7394–7403.
- [52] R. Wu, Q. Liao, X. Zhu, H. Wang, *Int. J. Heat Mass Tran.* 54 (2011) 4341–4348.
- [53] D. Shou, J. Fan, F. Ding, *J. Power Sources* 225 (2013) 179–186.
- [54] D.A.G. Bruggeman, *Annalen der Physik* (1935) 636–664, 5. Folge, Band 24.
- [55] Y. Utaka, *Int. J. Hydrogen Energy* 36 (2011) 9128–9138.
- [56] G.S. Hwang, A.Z. Weber, *J. Electrochem. Soc.* 159 (2012) F683–F692.
- [57] J.T. Gostick, M.A. Ioannidis, M.W. Fowler, M.D. Pritzker, *J. Power Sources* 173 (2007) 277–290.
- [58] N. Zamel, X. Li, J. Becker, A. Wiegmann, *Int. J. Hydrogen Energy* 36 (2011) 5466–5478.
- [59] J.T. Gostick, M.W. Fowler, M.D. Pritzker, M.A. Ioannidis, L.M. Behra, *J. Power Sources* 162 (2006) 228–238.
- [60] J.P. Feser, A.K. Prasad, S.G. Advani, *J. Power Sources* 162 (2006) 1226–1231.
- [61] I.S. Hussaini, C.-Y. Wang, *J. Power Sources* 195 (2010) 3830–3840.
- [62] A. Tamayol, M. Bahrami, *J. Power Sources* 196 (2011) 3559–3564.
- [63] A. Tamayol, F. McGregor, M. Bahrami, *J. Power Sources* 195 (2012) 94–99.
- [64] M. Kaviani, *Principles of Heat Transfer in Porous Media*, Springer-Verlag, USA, 1995.
- [65] X. Wang, T. Van Nguyen, D.S. Hussey, D.L. Jacobson, *J. Electrochem. Soc.* 157 (2010) B1777–B1782.
- [66] J. Roth, Doctoral dissertation, Universität Duisburg-Essen, Germany, 2010.
- [67] B. Ramos-Alvarado, J.D. Sole, A. Hernandez-Guerrero, M.W. Ellis, *J. Power Sources* 218 (2012) 221–232.
- [68] M. Reum, Doctoral dissertation, ETH Zurich, Switzerland, 2008.
- [69] J. Kleemann, F. Finsterwalder, W. Tillmetz, *J. Power Sources* 190 (2009) 92–102.
- [70] M.C. Leverett, *Trans. AIME* 142 (1941) 152–169.
- [71] W. Rose, W.A. Bruce, *Trans. AIME* 186 (1949) 127–142.
- [72] Z.H. Wang, C.-Y. Wang, K.S. Chen, *J. Power Sources* 94 (2001) 40–50.
- [73] K.S. Udell, *Int. J. Heat Mass Tran.* 28 (1985) 485–495.
- [74] J.T. Gostick, M.A. Ioannidis, M.W. Fowler, M.D. Pritzker, *J. Power Sources* 194 (2009) 433–444.
- [75] J.T. Gostick, M.A. Ioannidis, M.W. Fowler, D. Pritzker, in: U. Pasaogullari, C.-Y. Wang (Eds.), *Modeling and Diagnostics of Polymer Electrolyte Fuel Cells, Modern Aspects of Electrochemistry*, vol. 49, Springer, New York, USA, 2010, pp. 225–254.
- [76] E.C. Kumbur, K.V. Sharp, M.M. Mench, *J. Electrochem. Soc.* 154 (2007) B1315–B1324.
- [77] T.V. Nguyen, G. Lin, H. Ohn, X. Wang, *Electrochem. Solid St.* 11 (2008) B127–B131.
- [78] K.G. Gallagher, R.M. Darling, T.W. Patterson, M.L. Perry, *J. Electrochem. Soc.* 155 (2008) B1225–B1231.
- [79] I.R. Harkness, N. Hussain, L. Smith, J.D.B. Sharman, *J. Power Sources* 193 (2009) 122–129.
- [80] J.D. Fairweather, P. Cheung, D.T. Schwartz, *J. Power Sources* 195 (2010) 787–793.
- [81] L. Hao, P. Cheng, *Int. J. Heat Mass Tran.* 55 (2012) 133–139.
- [82] W.-W. Yang, T.-S. Zhao, C. Xu, *Electrochim. Acta* 53 (2007) 853–862.
- [83] J. Divisek, J. Fuhrmann, K. Gärtner, R. Jung, *J. Electrochem. Soc.* 150 (2003) A811–A825.
- [84] G. Murgia, L. Pisani, A.K. Shukla, K. Scott, *J. Electrochem. Soc.* 150 (2003) A1231–A1245.
- [85] D.L. Fritz III, J.S. Allen, *ECS Trans.* 25 (2009) 49–58.
- [86] S.H. Hun, Doctoral dissertation, The Pennsylvania State University, USA, 2010.
- [87] W. Liu, Doctoral dissertation, The Pennsylvania State University, USA, 2005.
- [88] HKS, ABAQUS v6.4 User's Manual, version 6.4 ed., ABAQUS Inc., Richmond, USA, 2003.
- [89] ANSYS FLUENT 13.0, ANSYS, Inc., Canonsburg, PA, USA, 2011.
- [90] C. Hartnig, I. Manke, J. Schloesser, P. Krüger, R. Kuhn, H. Riesemeier, K. Wippermann, J. Banhart, *Electrochem. Commun.* 11 (2009) 1559–1562.
- [91] A. Bazylak, D. Sinton, Z.-S. Liu, N. Djilali, *J. Power Sources* 163 (2007) 784–792.
- [92] Y. Gao, T.V. Nguyen, D.S. Hussey, D. Jacobson, *ECS Trans.* 33 (2010) 1435–1441.
- [93] F.M. White, *Fluid Mechanics*, fifth ed., McGraw-Hill, New York, USA, 2003.
- [94] C.L. Yaws, *Handbook of Transport Property Data: Viscosity, Thermal Conductivity and Diffusion Coefficients of Liquids and Gases*, Gulf Pub. Co., Houston, Texas, USA, 1995.
- [95] R.H. Perry, D.W. Green, J.O. Maloney, *Perry's Chemical Engineers' Handbook*, McGraw-Hill, New York, USA, 1984.
- [96] K. Scott, W.M. Taama, J. Cruickshank, *J. Power Sources* 65 (1997) 159–171.
- [97] H. Guo, C.F. Ma, *Electrochem. Commun.* 6 (2004) 306–312.
- [98] B.L. García, V.A. Sethuraman, J.W. Weidner, R.E. White, *J. Fuel Cell Sci. Technol.* 1 (2004) 43–48.